Available online at www.sciencedirect.com

SCIENCE DIRECT

Journal of Solid State Chemistry 177 (2004) 1886–1895

JOURNAL OF SOLID STATE CHEMISTRY

http://elsevier.com/locate/jssc

The phase diagram and tetragonal superstructures of the rare earth cobaltate phases $Ln_{1-x}Sr_xCoO_{3-\delta}$ ($Ln = La^{3+}$, Pr^{3+}, Nd^{3+}, Sm^{3+}, Gd^{3+}, Y^{3+}, Ho^{3+}, Dy^{3+}, Er^{3+}, Tm^{3+} and Yb^{3+})

M. James,[a,*] D. Cassidy,[b] D.J. Goossens,[a,c] and R.L. Withers[c]

[a] *Bragg Institute, Australian Nuclear Science and Technology Organisation, Neutron Scattering Group, Building 58, PMB 1, Menai NSW 2234, Australia*

[b] *Materials and Engineering Sciences, Australian Nuclear Science and Technology Organisation, PMB 1, Menai NSW 2234, Australia*

[c] *Research School of Chemistry, Australian National University, Canberra, ACT 0200, Australia*

Received 21 October 2003; received in revised form 5 January 2004; accepted 16 January 2004

Abstract

Single phase perovskite-based rare earth cobaltates ($Ln_{1-x}Sr_xCoO_{3-\delta}$) ($Ln = La^{3+}$, Pr^{3+}, Nd^{3+}, Sm^{3+}, Gd^{3+}, Dy^{3+}, Y^{3+}, Ho^{3+}, Er^{3+}, Tm^{3+} and Yb^{3+}; $0.67 \leqslant x \leqslant 0.9$) have been synthesized at 1100°C under 1 atmosphere of oxygen. X-ray diffraction of phases containing the larger rare earth ions La^{3+}, Pr^{3+} and Nd^{3+} reveals simple cubic structures; however electron diffraction shows orientational twinning of a local, tetragonal ($I4/mmm$; $a_p \times a_p \times 2a_p$) superstructure phase. Orientational twinning is also present for $Ln_{1-x}Sr_xCoO_{3-\delta}$ compounds containing rare earth ions smaller than Nd^{3+}. These compounds show a modulated intermediate parent with a tetragonal superstructure ($I4/mmm$; $2a_p \times 2a_p \times 4a_p$). Thermogravimetric measurements have determined the overall oxygen content, and these phases show mixed valence ($3^+/4^+$) cobalt oxidation states with up to 50% Co(IV). X-ray diffraction data and Rietveld techniques have been used to refine the structures of each of these tetragonal superstructure phases ($Ln = Sm^{3+}$–Yb^{3+}). Coupled Ln/Sr and oxygen/vacancy ordering and associated structural relaxation are shown to be responsible for the observed superstructure.

Keywords: Strontium doped cobaltate; Electron diffraction; Perovskite superstructure; Phase diagram

1. Introduction

Recently there has been a great deal of interest in rare earth cobaltate phases with perovskite structures ($Ln_{1-x}Sr_xCoO_{3-\delta}$) ($Ln$ = lanthanide ion), due to their applications in solid oxide fuel cells [1–4] and as ceramic membranes for high temperature oxygen separation [5,6]. The magnetic characteristics of these phases have also been the subject of frequent study as a consequence of their diverse behavior, including glassiness [7–9] and room temperature ferromagnetism [10–15]. Although the structure and physical properties of $La_{1-x}Sr_xCoO_{3-\delta}$, have been the subject of numerous investigations [3,16–21], studies of strontium-doped perovskite cobaltates based on the smaller lanthanide ions have only more recently become the subject of scrutiny [22–26].

Notably, large lanthanide elements such as La have been shown to react with other solid oxide fuel cell components such as yttria stabilized zirconia (YSZ) electrolyte to form stable low conductivity components such as $La_2Zr_2O_7$ and $SrZrO_3$ [27]. Lanthanide zirconate pyrochlores ($Ln_2Zr_2O_7$) have been shown to form only for Ln = La–Gd [28], and recent studies by Takeda and coworkers have demonstrated that smaller lanthanide cobaltates ($Ln_{1-x}Sr_xCoO_3$; Ln = Gd [29], Dy and Sm [2]) do not react with YSZ to form pyrochlores at 1000°C.

These attractive properties including the chemical stability of these materials are strongly dependent upon overall oxygen content as well as the ordering of oxygen vacancies or A-site cations. The amount and distribution of oxygen vacancies within the structure will affect the quantity and location of different cobalt oxidation states, and therefore impact significantly on

---

*Corresponding author. Fax: +61-2-9717-3606.
E-mail address: mja@ansto.gov.au (M. James).

0022-4596/$ - see front matter © 2004 Published by Elsevier Inc.
doi:10.1016/j.jssc.2004.01.012

the magnetic properties of these phases. Oxygen vacancy ordering and associated structural relaxation will also directly affect the potential for these materials to show oxygen ionic conductivity [3].

Our recent study revealed a series of new orthorhombic (but metrically tetragonal) perovskite superstructure phases $Ln_{0.33}Sr_{0.67}CoO_{3-\delta}$, ($Ln = Y^{3+}$, Ho^{3+} and Dy^{3+}) that result from a combination of oxygen vacancy and cation ordering [30]. In the following study we report the phase diagram of materials having this tetragonal crystal symmetry as a function of ionic radii and strontium doping levels and examine these effects upon the ensuing structures.

2. Experimental

2.1. Synthesis

Polycrystalline samples of $Ln_{1-x}Sr_xCoO_{3-\delta}$ were prepared from spectroscopic grade powders of $SrCO_3$ (98+%), $Co(NO_3)_2 \cdot 6H_2O$ (98%) and either Ln_2O_3 (Ln=La, Nd, Sm, Gd, Dy, Y, Er, Tm and Yb) ($\geqslant$99.9%), Pr_6O_{11} (99.9%) or $Ho(NO_3)_3 \cdot 5H_2O$ (99.9%). Samples were prepared for compositions with $x > 0.5$. The powders were dissolved in dilute nitric acid and an intimate mixture of the metal oxides was formed via the decomposition of a citric acid-ethylene glycol sol-gel. The residues were pelleted and sintered in a tube furnace at 1100°C under flowing oxygen for up to 3 days with intermediate re-grinding and re-pelleting until no further reaction was evident by powder X-ray diffraction. The samples were cooled from 1100°C to room temperature at a rate of 2°C per minute.

2.2. Thermogravimetry

Thermogravimetry of ca. 70 mg of each of the $Ln_{1-x}Sr_xCoO_{3-\delta}$ samples was carried out using a SETARAM TAG24 Simultaneous Thermogravimetric and Differential Thermal Analyser. The samples were reduced under a mixture of 3.5% hydrogen in nitrogen over a temperature range of 25–950°C at a heating rate of 5°C/min. Each of the samples studied decomposed under hydrogen reduction to give the component oxides Ln_2O_3 and SrO as well as Co metal. As has been shown for other rare earth perovskite cobaltates [31], the observed mass loss is therefore apportioned to the change in oxygen content as Co^{n+} in the as-synthesized sample is reduced to Co metal.

2.3. Electron diffraction

Electron diffraction (ED) was carried out using a Philips EM 430 Transmission Electron Microscope operating at 300 kV. Samples suitable for TEM work were prepared by the dispersion of finely ground material onto a holey carbon film.

2.4. Powder diffraction measurements

Powder X-ray diffraction measurements were made on a Scintag Inc. XGEN 4000 X-ray diffractometer at ambient temperature using Cu$K\alpha$ radiation and a flat-plate sample holder. Data of sufficient quality for structural refinement were collected over $5° < 2\Theta < 105°$, in 0.025° steps, with integration times of 10 s. Structure refinements were carried out by the Rietveld method [32] using the RIETICA program [33] with pseudo-Voigt peak shapes and refined backgrounds. Further details of the crystal structure investigations can be obtained from the Fachinformationszentrum Karlsruhe, 76344 Eggenstein-Leopoldshafen, Germany, (fax: +49-7247-808-66; E-mail: crysdata@fiz-karlsruhe.de). Depository numbers for single-phase samples are listed in Table 2.

3. Results and discussion

3.1. Powder X-ray diffraction (XRD)

Examination of X-ray diffraction data revealed a significant number of phases that crystallized with the modulated tetragonal ($I4/mmm$; $2a_p \times 2a_p \times 4a_p$) superstructure that we have previously reported for $Ln_{0.33}Sr_{0.67}CoO_{3-\delta}$ ($Ln = Dy^{3+}$, Y^{3+} and Ho^{3+}) [30]. In addition, we found that different solid solution ranges were present for $Ln_{1-x}Sr_xCoO_{3-\delta}$ depending on the lanthanide ion present. In general terms, samples based on La, Pr and Nd for $x \geqslant 0.67$ could be indexed on simple cubic ($Pm\bar{3}m$) parent perovskite structures and did not show diffraction peaks that could be attributed to the tetragonal superstructure phase. An X-ray diffraction pattern typical of these phases (that for $Pr_{0.10}Sr_{0.90}CoO_{3-\delta}$) is shown in Fig. 1(a). Table 1 lists the refined simple cubic cell parameters for the $x = 0.67$ and $x = 0.90$ compositions of compounds based on La, Pr and Nd.

X-ray diffraction profiles for $Ln_{1-x}Sr_xCoO_{3-\delta}$ compounds (Ln =Sm, Gd, Dy, Y and Ho) revealed single-phase samples that could all be indexed using the tetragonal ($I4/mmm$; $2a \times 2a \times 4a$) superstructure for $x = 0.67$. A typical X-ray diffraction pattern that shows tetragonal superstructure peaks (that for $Ho_{0.33}Sr_{0.67}CoO_{3-\delta}$) is shown in Fig. 1(b). The X-ray diffraction profiles of samples with nominal composition $Ln_{0.40}Sr_{0.60}CoO_{3-\delta}$ (Ln =Dy, Y and Ho) each showed the superstructure phase along with Ln_2O_3 as an impurity phase. It therefore seems evident that the lower solid solution limit for these compounds occurs between $x = 0.60$ and 0.67. Similarly, compounds with nominal composition $Ln_{0.33}Sr_{0.67}CoO_{3-\delta}$ containing the smaller

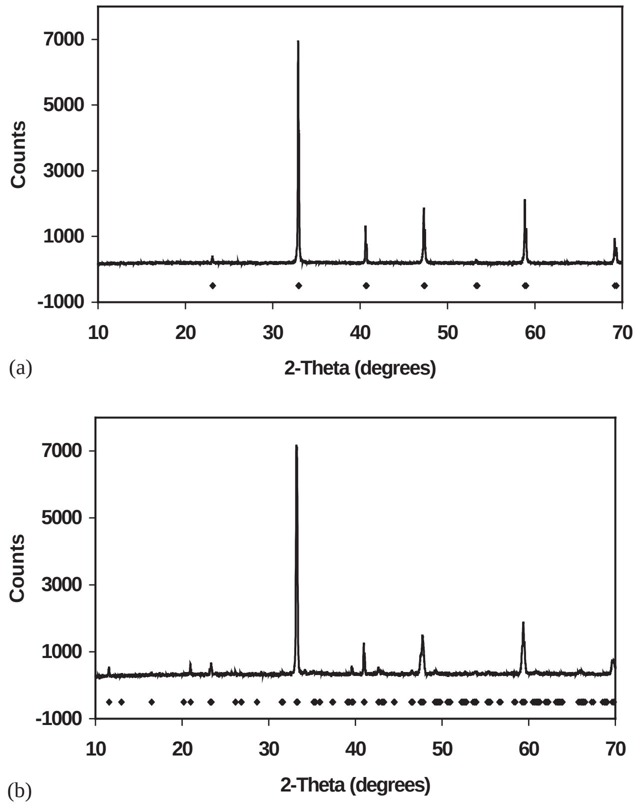

Fig. 1. X-ray diffraction profiles for (a) $Pr_{0.10}Sr_{0.90}CoO_{3-\delta}$ and (b) $Ho_{0.33}Sr_{0.67}CoO_{3-\delta}$.

Table 1
Refined simple perovskite unit cell parameters for $Ln_{1-x}Sr_xCoO_{3-\delta}$ (Ln =La, Pr and Nd; $x \geqslant 0.67$)

	a (Å)	V (Å^3)
$La_{0.33}Sr_{0.67}CoO_{3-\delta}$	3.8380(2)	56.535(6)
$La_{0.10}Sr_{0.90}CoO_{3-\delta}$	3.8424(1)	56.729(2)
$Pr_{0.33}Sr_{0.67}CoO_{3-\delta}$	3.8207(1)	55.773(2)
$Pr_{0.10}Sr_{0.90}CoO_{3-\delta}$	3.8370(1)	56.490(2)
$Nd_{0.33}Sr_{0.67}CoO_{3-\delta}$	3.8193(1)	55.713(1)
$Nd_{0.10}Sr_{0.90}CoO_{3-\delta}$	3.8396(2)	56.606(5)

lanthanide ions (Er, Tm and Yb) were not phase-pure, but formed the tetragonal superstructure phase in addition to Ln_2O_3 impurities.

With the exception of the phase based on Yb, each $Ln_{1-x}Sr_xCoO_{3-\delta}$ compound (Sm, Gd, Dy, Y, Ho, Er and Tm) formed single-phase samples without any Ln_2O_3 impurities for $x = 0.80$ and 0.90. In the case of the $Yb_{0.10}Sr_{0.90}CoO_{3-\delta}$ a very small amount of Yb_2O_3 (<1 molar percent) was found to be present. All of the $Ln_{1-x}Sr_xCoO_{3-\delta}$ ($x = 0.80$ and 0.90) phases listed above reveal diffraction peaks that are characteristic of these compounds crystallizing with the tetragonal superstructure; although in some instances for $x = 0.90$ the superstructure peaks are very weak.

The effect of increased Sr-doping on the crystal structures is clearly shown in the X-ray diffraction profiles for the $Sm_{1-x}Sr_xCoO_{3-\delta}$ series of phases ($x = 0.67$, 0.80 and 0.90) (Fig. 2(a)–(c)). The decrease in intensity of the weak superstructure peaks is clearly evident at higher Sr-doping levels, as is the reduction in tetragonal splitting with higher Sr content when one examines the parent perovskite $\langle 002 \rangle_p^*$ peak at $2\theta \sim 48°$.

3.2. Electron diffraction

In our previous study of the $Ln_{0.33}Sr_{0.67}CoO_{3-\delta}$ (Ln=Y^{3+}, Ho^{3+} and Dy^{3+}) doped rare earth cobaltates [30], electron diffraction was used to reveal a complex, previously unreported orthorhombic $Cmcm$ ($\boldsymbol{a} = 2\boldsymbol{a}_p - 2\boldsymbol{c}_p, \boldsymbol{b} = 4\boldsymbol{b}_p, \boldsymbol{c} = 2\boldsymbol{a}_p + 2\boldsymbol{c}_p$; subscript p for the perovskite parent structure) perovskite-related superstructure phase. It was further shown that there exists a strong F–centered subset of the corresponding Bragg reflections, belonging to an intermediate tetragonal 'parent' structure, associated with the above supercell. The weaker and somewhat streaked class of additional satellite reflections which lower the true resultant space group symmetry from F- to C-centered arise from a condensed $\boldsymbol{q} = \boldsymbol{c}*$ modulation of this intermediate tetragonal 'parent' structure. Indeed only these F-centered reflections could be observed at all in XRD patterns (this remains true for all the compositions investigated in the present study). Given the tetragonal metric symmetry observed by XRD for this composition, it was suggested that the intermediate 'parent' structure had tetragonal $F4/mmm$ symmetry (with the 4-fold axis running along $\boldsymbol{b}$). (The standard setting for this latter space group, $I4/mmm$, required a change in the above supercell setting to $\boldsymbol{a}' = 2\boldsymbol{a}_p, \boldsymbol{b}' = 2\boldsymbol{b}_p, \boldsymbol{c}' = 4\boldsymbol{c}_p$). It is this supercell that is apparent in XRD traces and that is referred to in the XRD section above and in what follows below.

As in our previous study, electron diffraction was again carried out on a number of samples where the weak nature of the superstructure reflections in the X-ray diffraction patterns made it difficult to distinguish between simple cubic and $I4/mmm$ tetragonal. Fig. 3a, for example, shows a commonly observed $\langle 001 \rangle_p$ type electron diffraction pattern (EDP) observed for $La_{0.1}Sr_{0.9}CoO_{3-\delta}$, $Pr_{0.1}Sr_{0.9}CoO_{3-\delta}$ and $Nd_{0.1}Sr_{0.9}CoO_{3-\delta}$. Note that the $\boldsymbol{G}_p \pm \frac{1}{2}[100]_p^*$ satellite reflections ($\boldsymbol{G}_p$ being a parent perovskite Bragg reflection) are much stronger than the very weakly present $\boldsymbol{G}_p \pm \frac{1}{2}[010]_p^*$ satellite reflections in Fig. 3(a). Such an observation is indicative of orientational twinning of a local, tetragonal ($a_p \times a_p \times 2a_p$) superstructure phase. Fig. 3(a) is in fact strongly reminiscent of a similar $\langle 001 \rangle_p$ type zone axis EPD previously reported for $La_{0.3}Sr_{0.7}CoO_{3-\delta}$ (cf. Fig. 3(a) with Fig. 6 of van Doorn and Burggraaf [3]).

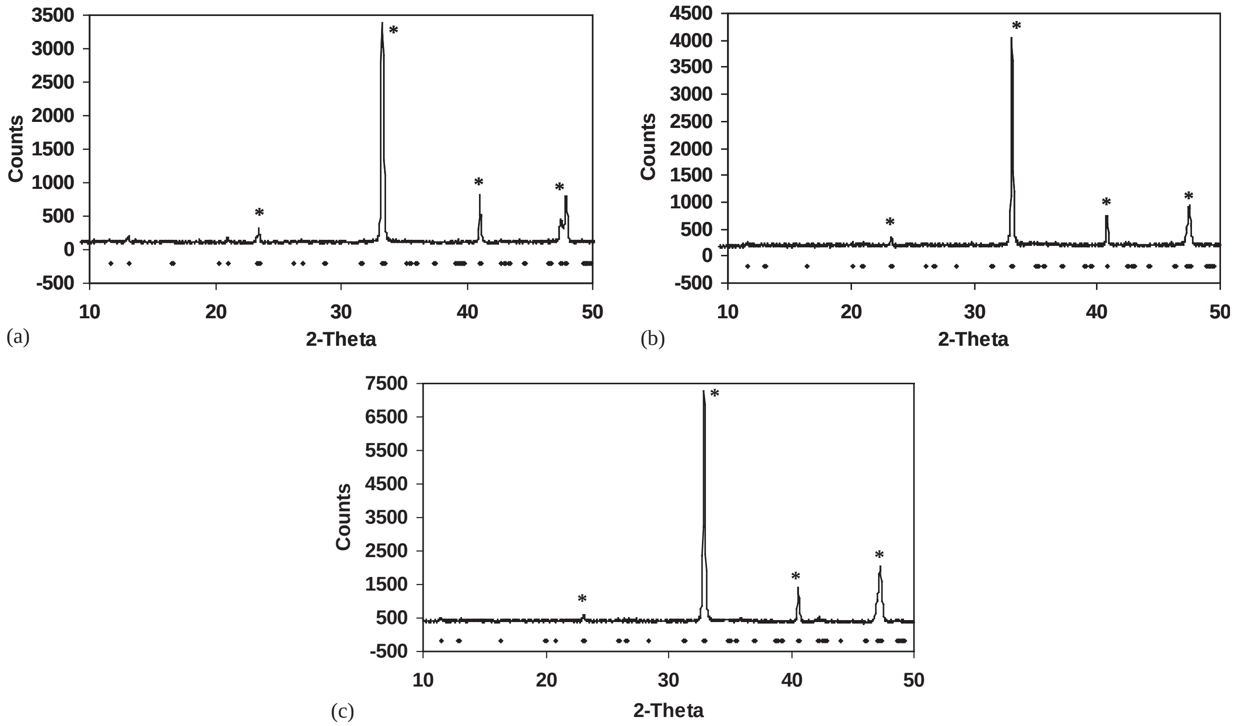

Fig. 2. X-ray diffraction profiles for (a) $Sm_{0.33}Sr_{0.67}CoO_{3-\delta}$, (b) $Sm_{0.20}Sr_{0.80}CoO_{3-\delta}$ and (c) $Sm_{0.10}Sr_{0.90}CoO_{3-\delta}$, indicating the reduction in superstructure peak intensity as well as tetragonal splitting. The parent perovskite peaks are indicated by "*".

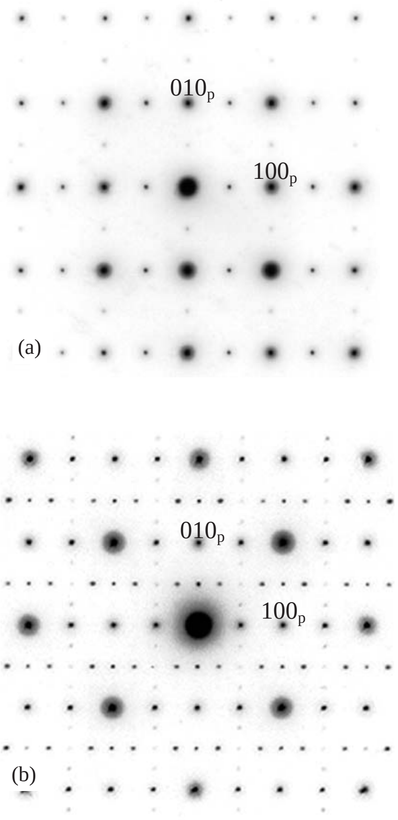

Fig. 3. Typical $\langle 001\rangle_p$ zone axis EDP of (a) $La_{0.10}Sr_{0.90}CoO_{3-\delta}$ and (b) $Y_{0.10}Sr_{0.90}CoO_{3-\delta}$.

Comparison of Fig. 3(a) and other obtained EDPs with the ED patterns and images observed by van Doorn and Burggraaf [3] suggest that these highly doped structures formed by the larger rare earth ions (La, Pr and Nd) are consistent with that reported for $La_{0.3}Sr_{0.7}CoO_{3-\delta}$.

By contrast, the typical $\langle 001\rangle_p$ zone axis EDP observed for $Y_{0.1}Sr_{0.9}CoO_{3-\delta}$ (see Fig. 3(b)) (and for all other rare earth ions from Sm to Yb) shows weak diffraction peaks that are characteristic of the ($I4/mmm$; $2a_p \times 2a_p \times 4a_p$) supercell (cf. Fig. 3(b) with Fig. 2(a) of [30]). Fig. 3(b) is in fact characteristic of an orientationally twinned tetragonal superstructure phase. In our previous investigation of this superstructure phase at the composition $Ln_{0.33}Sr_{0.67}CoO_{-\delta}$, it had proved possible to get inside a single domain region and thus obtain a single domain EDP. For the $Y_{0.1}Sr_{0.9}CoO_{3-\delta}$ composition, this did not prove possible as a result of the small domain size (~20–30 nm—see Fig. 4). Such a small domain size may well explain why the additional satellite reflections are not visible in either XRD or neutron powder diffraction patterns. Van Doorn and Burggraaf [3], for example, claim that microdomains with a size smaller than ~30 nm cannot be detected by means of powder XRD while Adler et al. [4] likewise claim that the minimum domain size which can be detected in neutron powder diffraction is ~200 nm.

One puzzling consequence of the present observations is that the same superstructure phase can apparently

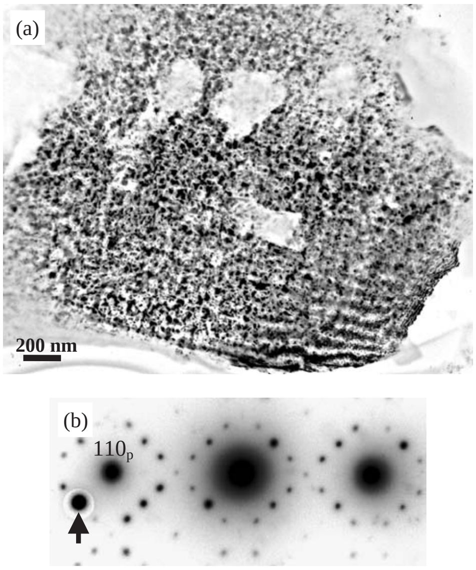

Fig. 4. (a) A typical $\mathbf{G}\pm\frac{1}{2}\langle 010\rangle_p^*$ satellite dark field image of a $Y_{0.10}Sr_{0.90}CoO_{3-\delta}$ specimen taken tilted a few degrees away from an $\langle 001\rangle$ zone axis orientation. The corresponding zone axis EDP and the satellite reflection used to form the image is shown in (b). The typical twin domain size is of the order of 20–30 nm.

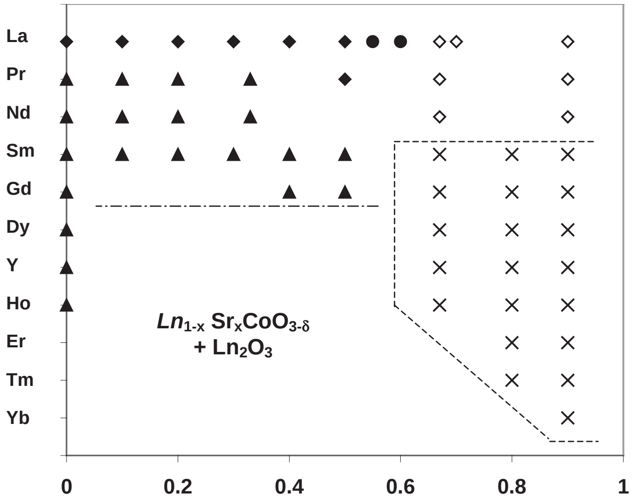

Fig. 5. The $Ln_{1-x}Sr_xCoO_{3-\delta}$ tetragonal superstructure phase diagram. Compositions having the metrically tetragonal ($I4/mmm$; $2a_p \times 2a_p \times 4a_p$) superstructure are shown by crosses ($\times$). Compositions having rhombohedral structures are indicated by ◆. Simple cubic structures are indicated by •. Metrically cubic structures with orientational twinning of a local tetragonal ($a_p \times a_p \times 2a_p$) superstructure are indicated by (◇). Orthorhombic structures are indicated by ▲.

exist despite the quite different Sr/*Ln* ratio for $x = 0.90$. This is puzzling because our previous investigation showed clearly that Sr/*Ln* ordering played an important role in the observed superstructure. (For a detailed analysis of the EDPs associated with the tetragonal superstructure phases the reader is referred to our previous study of the $Ln_{0.33}Sr_{0.67}CoO_{3-\delta}$ ($Ln = Y^{3+}$, Ho^{3+} and Dy^{3+}) members of this structural family [30]). It is therefore worth pointing out that a subtle but quite reproducible, structured diffuse intensity distribution is associated with the $x = 0.90$ samples but not with the $x = 0.67$ samples. The existence of this diffuse distribution may well be associated with the quite different Sr/*Ln* ratio for $x = 0.90$.

3.3. The $Ln_{1-x}Sr_xCoO_{3-\delta}$ perovskite phase diagram

Using the combination of X-ray and electron diffraction we are thus able to map out the phase diagram for pervoskite $Ln_{1-x}Sr_xCoO_{3-\delta}$ structures, the results of which we have summarized in Fig. 5. For the largest rare earth elements (La, Pr and Nd) an extended range of Sr-doping has previously been observed by a number of authors, although none of these compositions crystallized with the ($I4/mmm$; $2a_p \times 2a_p \times 4a_p$) tetragonal superstructure.

3.3.1. End member compositions: $LnCoO_3$ and "$SrCoO_{3-\delta}$"

Structures have been reported for un-doped end members $LnCoO_3$ for *Y* and most of the lanthanide elements. $LaCoO_3$ forms a rhombohedrally distorted structure (indicated by ◆ in Fig. 5) [19]. The smaller rare earth ions between Pr and Ho form orthorhombic $x = 0$ end members (indicated by ▲ in Fig. 5) [34–38].

Numerous references have been made in the literature to the $x = 1$ end member $SrCoO_{3-\delta}$ as crystallising with an orthorhombic, Brownmillerite structure (including those authors who report a complete solid solution ($0 \leqslant x \leqslant 1$) for some $Ln_{1-x}Sr_xCoO_{3-\delta}$ phases [2,22,23]). Our attempts to synthesize $SrCoO_{3-\delta}$ under the same conditions as our $Ln_{1-x}Sr_xCoO_{3-\delta}$ phases led to the formation of the compound $Sr_6Co_5O_{15}$ that has a trigonal crystal structure (as determined by Harrison and coworkers using powder neutron diffraction [39]) along with a small amount of Co_3O_4.

3.3.2. $Ln_{1-x}Sr_xCoO_{3-\delta}$ structures formed by large lanthanide ions (Ln=La–Gd)

Numerous authors have studied the structural variation of $La_{1-x}Sr_xCoO_{3-\delta}$ as a function of Sr-doping [3,25,40–44]. These studies are in agreement that $La_{1-x}Sr_xCoO_{3-\delta}$ phases form rhombohedrally distorted cubic perovskite phases for $x \leqslant 0.5$ (◆). Earlier studies of $La_{1-x}Sr_xCoO_{3-\delta}$ for $x > 0.5$ reported simple cubic ($Pm\bar{3}m$) pervoskite structures (•) [41–43]. More recently, van Doorn and Burggraaf have demonstrated for $La_{0.3}Sr_{0.7}CoO_{3-\delta}$ using X-ray, neutron and electron diffraction that distinct microdomians were present with a tetragonal $a_p \times a_p \times 2a_p$ superstructure as well as regions without such a superstructure (◇). They determined that the superstructure could be rationalized by removal of the oxygen atoms and formation of vacancies in every second (001) (La/Sr)O plane [3]. The upper limits to the solid solution have been reported to occur between 0.7 [42–43] and 0.8 [3,44], depending upon the preparation methods. In the case of our own study, X-ray and electron diffraction of samples produced via sol-gel methods under 1 atmosphere of oxygen indicate a single phase composition for $x = 0.90$. In the light of our own electron diffraction results we conclude that our $La_{0.10}Sr_{0.90}CoO_3$ sample also forms this tetragonal ($a_p \times a_p \times 2a_p$) superstructure (indicated by $\diamondsuit$ in Fig. 5).

Prior studies of $Pr_{1-x}Sr_xCoO_{3-\delta}$ [25,38,45] and $Nd_{1-x}SrCoO_{3-\delta}$ [25,45–46] phases also show transformations from orthorhombic structures (▲) for $x \leqslant 0.33$ [38–46] to rhombohedral crystal symmetry (◆) for $x = 0.5$ [25]. Brinks and co-authors by way of contrast reported a monoclinic structure for $Pr_{0.5}Sr_{0.5}CoO_{3-\delta}$ [38]. Although our own X-ray diffraction results suggest single phase simple cubic samples for both Pr and Nd phases from $x = 0.67$ to $x = 0.90$, electron diffraction reveals microdomains of ordered oxygen vacancies and a ($a_p \times a_p \times 2a_p$) tetragonal superstructure ($\diamondsuit$) of the type observed for highly doped $La_{1-x}Sr_xCoO_{3-\delta}$.

A number of authors have reported a complete solid solution ($0<x<1$) for $Sm_{1-x}Sr_xCoO_{3-\delta}$ [2,23] and $Gd_{1-x}Sr_xCoO_{3-\delta}$ [22,29] synthesized in air at 1200°C. Tu and co-workers reported orthorhombic structures (▲) for $Sm_{1-x}Sr_xCoO_{3-\delta}$ at compositions $x \leqslant 0.5$ and cubic phases for $x \geqslant 0.6$ [2], while Kang et al. found structural transitions from orthorhombic ($x = 0.25$) to cubic ($x = 0.5$) to tetragonal ($x = 0.75$) [23]. Ryu and co-workers reported the same structural transitions for $Gd_{1-x}Sr_xCoO_{3-\delta}$ [22], however Takeda et al. reported a two-phase region below $x = 0.4$ and cubic region for $x \geqslant 0.4$ [29]. Although both groups sintered their samples at 1200°C in air, the fact that Ryu and coworkers did not report a two-phase region might result from their use of nitrate precursors [22] as opposed to the use of a standard solid state process by Takeda et al. [29]. In each of the above studies, the authors provided unit cell parameters for these phases, however they did not present their X-ray diffraction data nor offer any further structural details. In those instances where tetragonal phases were reported, the lattice parameters for $Sm_{0.25}Sr_{0.75}CoO_{3-\delta}$ and $Gd_{0.25}Sr_{0.75}CoO_{3-\delta}$ were both indexed on the basis of different tetragonal unit cells to that which we observed ($a = 10.877$ Å, $c = 7.716$ Å [23] and $a = 3.849$ Å, $c = 3.846$ Å [22], respectively).

3.3.3. The tetragonal ($2a_p \times 2a_p \times 4a_p$) superstructure phase (Ln=Sm–Yb)

Two previous studies have investigated the structural behavior of $Dy_{1-x}Sr_xCoO_{3-\delta}$ as a function of Sr-doping. Jeong et al. reported a solid solution from $0 \leqslant x \leqslant 1$ for $Dy_{1-x}Sr_xCoO_{3-\delta}$ prepared at 1000°C [24]. They observed an orthorhombic phase at $x = 0.25$ similar to the ($x = 0$) end member $DyCoO_3$, and tetragonal structures at $x = 0.5$ and 0.75. Careful examination of their XRD patterns and lattice parameters clearly show that they do not have single-phase samples over the entire "solid solution" range. Both the $x = 0.25$ and 0.50 compositions appear to be mixtures of the (orthorhombic) $DyCoO_3$ [37] and tetragonal phases and the variation in their lattice parameters for these compositions are not sufficient to explain the apparent splitting displayed in their XRD data. In agreement with our own results, Tu and coworkers observed a single-phase region for $Dy_{1-x}Sr_xCoO_{3-\delta}$ for $0.6<x \leqslant 0.9$ [2], although they characterized these phases as forming simple cubic perovskite structures. It seems evident that $Dy_{1-x}Sr_xCoO_{3-\delta}$ compositions for small x form $DyCoO_3$ with additional impurity phases, while compositions for $x>0.6$ form the tetragonal superstructure phase and a two-phase region exists for intermediate compositions.

Our previous study [30] revealed that the ($2a_p \times 2a_p \times 4a_p$) tetragonal superstructure was formed for $Ln_{0.33}Sr_{0.67}CoO_{3-\delta}$, ($Ln = Y^{3+}$, Ho^{3+} and Dy^{3+}). Istomin et al. subsequently confirmed the same tetragonal structure was formed for $Y_{0.3}Sr_{0.7}CoO_{2.62}$, although they did not observe any A-site Y/Sr ordering [47]. Our present investigation using X-ray and electron diffraction indicates that the same tetragonal superstructure is formed for the rare earth elements smaller than Nd (see Fig. 5). In the case of Sm, Gd, Dy, Y and Ho the structure type exists for compositions $0.6<x \leqslant 0.9$. For lanthanide elements smaller than Ho, the solid solution range shrinks for Er, Tm ($0.80 \leqslant x \leqslant 0.90$) and Yb ($x = 0.90$).

3.4. Thermogravimetry

The overall oxygen content and average cobalt oxidation state for each single-phase sample was determined using thermogravimetric analysis and these results are given in Table 2. A typical weight-loss spectrum (that of $Sm_{0.2}Sr_{0.8}CoO_{3-\delta}$), is shown in Fig. 6. Each of the thermogravimetric profiles show two intermediate weight-loss plateaus between the as-prepared cobalt oxidation state and the fully reduced cobalt metal. The first plateau appears representative of an intermediate Co(III) oxidation state, while the second plateau appears between Co(II) and Co(I).

Despite significant variation in the level of Sr-doping of the $Ln_{1-x}Sr_xCoO_{3-\delta}$ phases from $x = 0.67$ to 0.90, little overall variation in oxygen content was observed ($\delta = 0.18$ for $Gd_{0.33}Sr_{0.67}CoO_{3-\delta}$ to $\delta = 0.31$ for $Y_{0.2}Sr_{0.8}CoO_{3-\delta}$). Furthermore, examination of Table 2 shows that there is no systematic variation in the amount of oxygen vacancies as a function of Sr-doping for a given lanthanide ion. In general terms, the oxygen

Table 2
Oxygen content, average cobalt oxidation state (Co^{n+}) and CSD depository numbers for $Ln_{1-x}Sr_xCoO_{3-\delta}$ tetragonal superstructure phases (Ln =Sm–Yb)

	$x = 0.67$	$x = 0.80$	$x = 0.90$
$Sm_{1-x}Sr_xCoO_{3-\delta}$			
Oxygen content	2.80	2.79	2.76
% Co^{4+}	27	38	43
CSD-#			
$Gd_{1-x}Sr_xCoO_{3-\delta}$			
Oxygen content	2.82	2.72	2.76
% Co^{4+}	31	23	42
CSD-#			
$Dy_{1-x}Sr_xCoO_{3-\delta}$			
Oxygen content	2.78	2.71	2.79
% Co^{4+}	23	21	48
CSD-#			
$Y_{1-x}Sr_xCoO_{3-\delta}$			
Oxygen content	2.79	2.69	2.77
% Co^{4+}	25	31	45
CSD-#			
$Ho_{1-x}Sr_xCoO_{3-\delta}$			
Oxygen content	2.76	2.75	2.79
% Co^{4+}	19	30	47
CSD-#			
$Er_{1-x}Sr_xCoO_{3-\delta}$			
Oxygen content		2.74	2.78
% Co^{4+}		27	45
CSD-#			
$Tm_{1-x}Sr_xCoO_{3-\delta}$			
Oxygen content		2.73	2.81
% Co^{4+}		25	51
CSD-#			
$Yb_{1-x}Sr_xCoO_{3-\delta}$			
Oxygen content			2.78
% Co^{4+}			46
CSD-#			

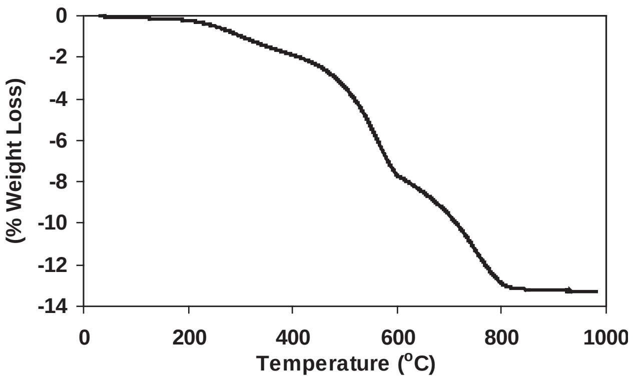

Fig. 6. The thermogravimetric weight-loss spectrum of $Sm_{0.2}Sr_{0.8}CoO_{2.79}$.

content of each of these phases appears to be more a function of the sintering conditions than the crystal chemistry. While the level of oxygen vacancies present in these phases is quite high (up to ~10%), it is consistent with the behavior observed at similar Sr^{2+} doping levels in other perovskite-based rare earth cobaltates [22–24].

In contrast, the average cobalt oxidation state of these phases is heavily influenced by the level of strontium doping. The average oxidation state of the $Ln_{0.33}Sr_{0.67}CoO_{3-\delta}$ phases was found to be 3.25, that for the $Ln_{0.20}Sr_{0.80}CoO_{3-\delta}$ phases was 3.28 while the average oxidation state for $Ln_{0.10}Sr_{0.90}CoO_{3-\delta}$ was substantially higher at 3.46. The amount of Co^{4+} in these phases varies from 19% for $Ho_{0.33}Sr_{0.66}CoO_{2.76}$ to 51% for $Tm_{0.10}Sr_{0.90}CoO_{2.81}$. Although not the subject of this study, we have demonstrated that the variation in Co^{4+} content in these phases has a profound affect on the magnetic properties of these superstructure compounds [48].

3.5. Structural variation in the tetragonal ($2a_p \times 2a_p \times 4a_p$) superstructure phase

The structures of compositions forming the tetragonal ($2a_p \times 2a_p \times 4a_p$) superstructure phase were refined using X-ray diffraction data and the Rietveld method for $Ln_{1-x}Sr_xCoO_{3-\delta}$ (Ln =Sm, Gd, Dy, Y, Ho, Er, Tm and Yb). The initial positions of atoms were based on the structures of $Ln_{0.33}Sr_{0.67}CoO_{3-\delta}$ determined in our earlier work [30]. For the initial refinements, the relative site occupancies were set at their nominal compositions, with the Sr^{2+} and rare earth (Ln^{3+}) ions disordered over the three distinct sites in this $I4/mmm$ supercell. The oxygen sites were initially set as fully occupied. Refinement of isotropic thermal parameters indicated sites where substantial oxygen deficiency and/or Sr^{2+}/Ln^{3+} disorder were present.

Refined lattice parameters for each for $Ln_{1-x}Sr_xCoO_{3-\delta}$ composition are listed in Table 3. Several different competing processes occur as a function of Sr-doping that may affect the dimensions of the crystal lattice. Oxidation of Co^{3+} to Co^{4+} is accompanied by a reduction in ionic radii from 0.61 to 0.53 Å [49]. In general, we observed little difference in cobalt oxidation between $x = 0.67$ and 0.80 compositions however the amount of oxidation becomes more significant for the $x = 0.90$ phases. Given the change in average oxidation state from 3.25 for $Ln_{0.33}Sr_{0.67}CoO_{3-\delta}$ compounds to 3.46 for $Ln_{0.10}Sr_{0.90}CoO_{3-\delta}$ materials however, one would only expect a reduction in average cobalt ionic radii from ~0.59 Å to ~0.57 Å.

A further process that would affect the crystal dimension is an increase in size due to structural relaxation associated with oxygen vacancies. As shown in Table 2 however there appears to be little variation in

Table 3
Unit cell parameters for $Ln_{1-x}Sr_xCoO_{3-\delta}$ tetragonal superstructure phases (*Ln* =Sm–Yb)

	$x = 0.67$	$x = 0.80$	$x = 0.90$
$Sm_{1-x}Sr_xCoO_{3-\delta}$			
a (Å)	7.6149(4)	7.6724(4)	7.6968(8)
c (Å)	15.3472(10)	15.3983(11)	15.4672(16)
V (Å^3)	889.93(9)	906.44(9)	916.30(16)
C/2*a*	1.0077	1.0034	1.0048
$Gd_{1-x}Sr_xCoO_{3-\delta}$			
a (Å)	7.6228(1)	7.6720(5)	7.6900(3)
c (Å)	15.3733(3)	15.4232(11)	15.4210(8)
V (Å^3)	893.30(3)	907.81(10)	911.94(7)
C/2*a*	1.0084	1.0052	1.0027
$Dy_{1-x}Sr_xCoO_{3-\delta}$			
a (Å)	7.6091(2)	7.6688(5)	7.6971(6)
c (Å)	15.3398(5)	15.3888(15)	15.4237(14)
V (Å^3)	888.15(4)	905.02(13)	913.79(14)
	1.0080	1.0033	1.0019
$Y_{1-x}Sr_xCoO_{3-\delta}$			
a (Å)	7.6227(3)	7.6637(4)	7.6918(4)
c (Å)	15.3188(8)	15.3761(8)	15.4099(11)
V (Å^3)	890.10(7)	903.04(8)	911.70(10)
	1.0048	1.0032	1.0017
$Ho_{1-x}Sr_xCoO_{3-\delta}$			
a (Å)	7.6134(3)	7.6676(4)	7.6895(2)
c (Å)	15.3001(8)	15.3844(10)	15.4008(6)
V (Å^3)	886.85(7)	904.47(8)	910.62(5)
	1.0048	1.0032	1.0014
$Er_{1-x}Sr_xCoO_{3-\delta}$			
a (Å)		7.6643(4)	7.6812(2)
c (Å)		15.3730(12)	15.3755(5)
V (Å^3)		903.03(10)	907.17(4)
		1.0029	1.0009
$Tm_{1-x}Sr_xCoO_{3-\delta}$			
a (Å)		7.6591(4)	7.6965(2)
c (Å)		15.3514(10)	15.4031(6)
V (Å^3)		900.54(9)	912.43(5)
		1.0022	1.0007
$Yb_{1-x}Sr_xCoO_{3-\delta}$			
a (Å)			7.6813(2)
c (Å)			15.3706(7)
V (Å^3)			906.89(5)
			1.0005

the amount of oxygen vacancies present in these materials as a function of Sr-doping.

The most significant factor in driving an increase in cell dimension with an increase in Sr content is the actual size difference between the rare earth ions and Sr^{2+} itself. For those rare earths with an extended solid solution range (Sm–Ho: $0.67 \leqslant x \leqslant 0.9$), the difference in ionic radii between Sr^{2+} (1.44 Å) and Sm^{3+} (1.24 Å) or Ho^{3+} (1.18 Å) is considerable (>15%) [49]. In the case of the latter, one would envisage the average Ho/Sr site radius to expand from 1.35 Å to 1.41 Å. As is expected from the above discussion, we observed substantial lattice expansion (~23.9 Å^3 in that case of $Ho_{1-x}Sr_xCoO_{3-\delta}$) between $x = 0.67$ and 0.90.

Examination of the $c/2a$ ratio for each $Ln_{1-x}Sr_xCoO_{3-\delta}$ composition (Table 3) reveals that the tetragonal splitting of the structure decreases with increasing Sr-doping, giving a progressive shift towards a cubic lattice (e.g. 1.0084 for $Gd_{0.33}Sr_{0.67}CoO_{3-\delta}$ to 1.0027 for $Gd_{0.10}Sr_{0.90}CoO_{3-\delta}$). Although the tetragonal splitting becomes increasingly difficult to visualize in the XRD profiles, the presence of the tetragonal superstructure peaks for $Ln_{0.10}Sr_{0.90}CoO_{3-\delta}$ compositions along with confirmation from electron diffraction supports the refinement of these structures in the $I4/mmm$ space group. In addition to tetragonal variation as a function of Sr-doping, there also is a decrease in splitting with decreasing ionic radius of the rare earth ion. This is particularly evident when one examines the $Ln_{0.10}Sr_{0.90}CoO_{3-\delta}$ phases, ranging from 1.0048 for $Sm_{0.10}Sr_{0.90}CoO_{3-\delta}$ to 1.0005 for $Yb_{0.10}Sr_{0.90}CoO_{3-\delta}$.

The observed, calculated and difference XRD profiles of a typical sample ($Ho_{0.10}Sr_{0.90}CoO_{3-\delta}$) is shown in Figs. 7 and 8, while the refined atomic positions and thermal parameters for this compound are given in Table 4. Although the atomic positions and thermal parameters for the other isostructural members of the tetragonal superstructure phase are not listed here, they may be obtained from the Fachinformationszentrum Karlsruhe (see above).

The refined structure for each $Ln_{1-x}Sr_xCoO_{3-\delta}$ phase that forms the tetragonal superstructure corresponds to the ones that we have previously described [30]. The relative occupation of the different *Ln*/Sr sites in these structures was found to vary as a function of Sr-doping (i.e. with *x*). For the $x = 0.67$ compositions the *Ln*/Sr1 sites were fully occupied by Ln^{3+} ions, the *Ln*/Sr2 sites were fully occupied by Sr^{2+} ions and the remaining Ln^{3+} ions were disordered with Sr^{2+} over the *Ln*/Sr3 sites. For both the $x = 0.80$ and 0.90 compositions, the *Ln*/Sr1 sites were found to contain both Ln^{3+} and Sr^{2+} ions, while the *Ln*/Sr2 and *Ln*/Sr3 sites were found to be fully occupied by Sr^{2+} ions. For the $Y_{1-x}Sr_xCoO_{3-\delta}$ series of compounds, the relative occupancy of the Y/Sr sites were unable to be determined from the XRD data as no scattering contrast exists between isoelectronic

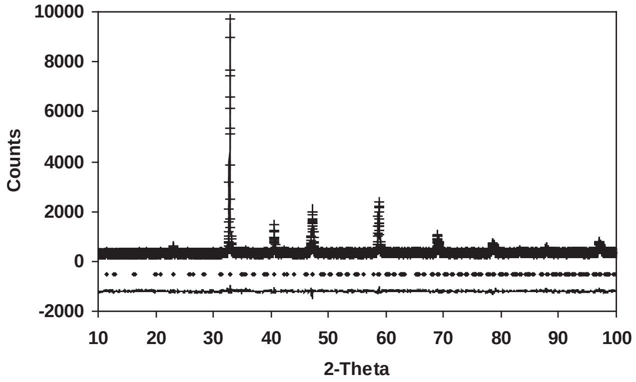

Fig. 7. The observed (+), calculated and difference X-ray diffraction profiles for $Ho_{0.10}Sr_{0.90}CoO_{2.79}$.

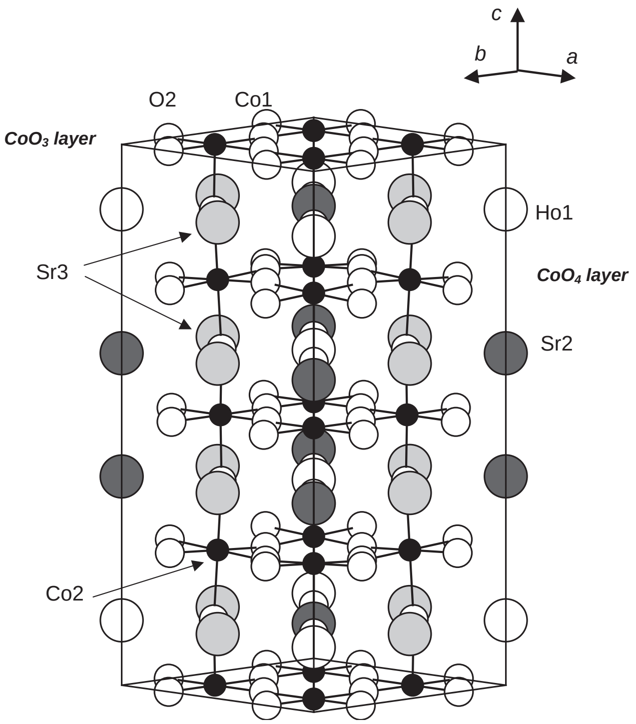

Fig. 8. The refined structure of $Ho_{0.10}Sr_{0.90}CoO_{2.79}$ in a projection close to the supercell $\langle 110 \rangle$ direction. Note the CoO_3 layers at $z = 0$ and $\frac{1}{2}$ and the CoO_4 layers at $z = \frac{1}{4}$ and $\frac{3}{4}$. Approximately 50% of the O2 sites are vacant. The rare earth layers contains disordered Sr/*Ln*1 ions (in the ratio 6:4), Sr2 ions and Sr3 ions.

Table 4
Refined atomic positions and thermal parameters (B_{iso}; $Å^2 \times 100$) for the $Ho_{0.10}Sr_{0.90}CoO_{2.79}$ tetragonal superstructure phase

Atom	Site	x	y	z	B_{iso}	Occ.
Co1	8*h*	0.2428(8)	0.2428(8)	0	2.01(7)	1
Co2	8*f*	$\frac{1}{4}$	$\frac{1}{4}$	$\frac{1}{4}$	2.01(7)	1
Ho1/Sr1	4*e*	0	0	0.1200(9)	2.45(5)	
Sr2	4*e*	0	0	0.6139(10)	2.45(5)	1
Sr3	8*g*	0	$\frac{1}{2}$	0.1195(6)	2.45(5)	1
O1	16*m*	0.240(1)	0.240(1)	0.122(1)	4.0(2)	1
O2	8*i*	0.245(2)	0	0	4.0(2)	0.58
O3	8*j*	0.240(1)	$\frac{1}{2}$	0	4.0(2)	1
O4	16*n*	0	0.251(1)	0.257(1)	4.0(2)	1

$R_P = 4.8$; $R_{WP} = 6.1$; $R_B = 2.3$.

Y^{3+} and Sr^{2+} ions. For these compounds it was assumed that the site occupancies followed the same trends as the compounds containing the heavier lanthanide ions.

Determination of the occupancy of the oxygen sites using XRD data is a difficult prospect given the relative scattering power of oxygen atoms or vacancies and the substantially heavier metal ions in the structure. Examination of the oxygen site thermal parameters however did give a clear indication of those sites where substantial disorder between oxygen and vacancies was present.

For $x = 0.67$ compositions, the oxygen vacancies appear to be localized on the O2 sites. Given the strong correlations that were present between site occupation factors and isotropic thermal parameters, as well as the relatively weak scattering power of oxygen atoms, the O2 site occupation factors were set at the value determined by thermogravimetry. Although our study shows substantial disorder on this oxygen site, the exact nature of the oxygen coordination in these phases will ultimately require study using neutron diffraction.

The impact of the observed A-site cation ordering on the *Ln*/Sr–O bond lengths of the structure become more obvious as the size of the rare earth ion decreases. Little difference is apparent between the average Sm/Sr1–O, Sm/Sr2–O and Sm/Sr3–O bond lengths for $Sm_{0.33}Sr_{0.67}CoO_{2.80}$ (2.704, 2.654 and 2.722 Å, respectively). The average bond lengths for $Ho_{0.33}Sr_{0.67}CoO_{2.76}$ (2.556, 2.772 and 2.721 Å) however, clearly correlate with the preferential ordering of Ho onto the Ho1 and Ho/Sr3 sites. For high Sr-doping levels ($x = 0.90$), the average *Ln*/Sr–O*n* bond lengths do not decrease in any systematic manner as a function decreasing rare earth radii. This is not unexpected. Based on Shannon's ionic radii [49] one would expect only a 0.02 Å decrease in *Ln*/Sr1–O bond length between $Sm_{0.10}Sr_{0.90}CoO_{2.80}$ and $Yb_{0.10}Sr_{0.90}CoO_{2.78}$.

The results of the structure refinements provide an indication that charge ordering is taking place between Co1 and Co2 sites. If ordering was taking place between Co(III) and Co(IV), it would be expected that Co^{4+}–O bonds should be substantially shorter (~1.93 Å) than Co^{3+}–O bonds (~2.01 Å) [49]. While the Co1–O bonds tend to be consistently shorter than the Co2–O bonds for the whole range of $Ln_{1-x}Sr_xCoO_{3-\delta}$ compositions, the difference is most pronounced for the $Ln_{0.10}Sr_{0.90}CoO_{3-\delta}$ series. The average Co1–O bond length is 1.889 Å, while the Co2–O bond length is 1.975 Å. Given that the average oxidation state of the $Ln_{0.10}Sr_{0.90}CoO_{3-\delta}$ series is 3.46+ and that two cobalt sites have equal multiplicity, it seems reasonable that Co^{4+} should exclusively occupy the smaller Co1 site.

4. Conclusions

We have determined the phase boundaries of the tetragonal ($I4/mmm$; $2a_p \times 2a_p \times 4a_p$) superstructure phase for $Ln_{1-x}Sr_xCoO_{3-\delta}$ ($Ln = Sm^{3+}$–Yb^{3+}; $0.67 \leqslant x \leqslant 0.9$). In doing so we have mapped out the phase diagram of these strontium-doped, rare earth cobaltates and shown that the range of solid solution for these phases becomes smaller with decreasing ionic radii. Highly doped phases containing the larger rare earth ions La^{3+}, Pr^{3+} and Nd^{3+} show simple cubic structures with orientational twinning of a local, tetragonal ($I4/mmm$; $a_p \times a_p \times 2a_p$) superstructure phase. These phases show mixed valence (3+/4+) cobalt oxidation states with up to 50% Co(IV). The tetragonal superstructure phases for $Ln_{1-x}Sr_xCoO_{3-\delta}$ ($Ln=Sm^{3+}$–Yb^{3+}) show both Ln/Sr and oxygen vacancy ordering.

Acknowledgments

RLW and DJG acknowledge the Australian Research Council (ARC) for financial support in the form of ARC Discovery Grants.

References

[1] S.J. Skinner, Int. J. Inorg. Mater. 3 (2001) 113.

[2] H.Y. Tu, Y. Takeda, N. Imanishi, O. Yamamoto, Solid State Ionics 100 (1997) 283.

[3] R.H.E. van Doorn, A.J. Burggraaf, Solid State Ionics 128 (2000) 65.

[4] S.B. Adler, Solid State Ionics 111 (1998) 111.

[5] A.V. Kovalevsky, V.V. Kharton, V.N. Tikhonovich, E.N. Naumovich, A.A. Tonoyan, O.P. Reut, L.S. Boginsky, Mater. Sci. Eng. B 52 (1998) 105.

[6] V.V. Kharton, A.A. Yaremchenko, A.V. Kovalevsky, A.P. Viskup, E.N. Naumovich, P.F. Kerko, J. Membrane Sci. 163 (1999) 307.

[7] S. Mukherjee, R. Ranganathan, P.S. Anikumar, P.A. Joy, Phys. Rev. B 54 (1996) 9367.

[8] P.S. Anil Kumar, P.A. Joy, S.K. Date, J. Phys.: Condens. Matter 10 (1998) L487.

[9] D.N.H. Nam, K. Jonason, P. Nordblad, N.V. Khiem, N.X. Phuc, Phys. Rev. B 59 (1998) 4189.

[10] K. Asai, O. Yokokura, N. Nishimori, H. Chou, J.M. Tranquada, G. Shirane, S. Higuchi, Y. Okajima, K. Kohn, Phys. Rev. B 50 (1994) 3025.

[11] M.A. Senaris-Rodriguez, J.B. Goodenough, J. Solid State Chem. 118 (1995) 323.

[12] R. Caciuffo, D. Rinaldi, G. Barucca, J. Mira, J. Rivas, M.A. Senaris-Rodriguez, P.G. Radaelli, D. Fiorani, J.B. Goodenough, Phys. Rev. B 59 (1999) 1068.

[13] J. Mira, J. Rivas, M. Vazquez, J.M. Garcia-Beneytez, J. Arcas, R.D. Sanchez, M.A. Senaris-Rodriguez, Phys. Rev. B 59 (1999) 123.

[14] R. Ganguly, I.K. Gopalakrishnan, J.V. Yakhmi, Physica B 271 (1999) 116.

[15] Sujeet. Chaudhary, S.B. Roy, P. Chaddah, J. Alloys Compd. 326 (2001) 112.

[16] G.H. Jonker, J.H. Van Santen, Physica 19 (1953) 120.

[17] J.B. Goodenough, J. Phys. Chem. Solids 6 (1958) 287.

[18] P.M. Raccah, J.B. Goodenough, J. Appl. Phys. 39 (1968) 1209.

[19] G. Thornton, B.C. Tofield, A.W. Hewat, J. Solid State Chem. 61 (1986) 301.

[20] J. Mizusaki, J. Tabuchi, T. Matsuura, S. Yamauchi, K. Fueki, J. Electrochem. Soc. 136 (1989) 2082.

[21] M.A. Senaris-Rodriguez, M.P. Breijo, S. Castro, C. Rey, M. Sanchez, R.D. Sanchez, J. Mira, A. Fondado, J. Rivas, Int. J. Inorg. Mater. 1 (1999) 281.

[22] K.H. Ryu, K.S. Roh, S.J. Lee, C.H. Yo, J. Solid State Chem. 105 (1993) 550.

[23] J.W. Kang, K.H. Ryu, C.H. Yo, Bull. Korean Chem. Soc. 17 (1995) 600.

[24] S.K. Jeong, M.G. Kim, K.H. Kim, C.H. Yo, Bull. Korean Chem. Soc. 17 (1996) 794.

[25] P.V. Vanitha, A. Arulraj, P.N. Santhosh, C.N.R. Rao, Chem. Mater. 12 (2000) 1666.

[26] K. Yoshii, H. Abe, A. Nakamura, Mat. Res. Bull. 36 (2001) 1477.

[27] O. Yamamoto, Y. Takeda, R. Kanno, N. Noda, Solid State Ionics 22 (1987) 241.

[28] M.A. Subramanan, G. Aravamdam, G.V. Subba Rao, Prog. Solid State Chem. 15 (1983) 55.

[29] Y. Takeda, H. Ueno, N. Imanishi, O. Yamamoto, N. Sammes, M.B. Philipps, Solid State Ionics 86–88 (1996) 1187.

[30] R.L. Withers, M. James, D.J. Goossens, J. Solid State Chem. 174 (1) (2003) 198–208.

[31] M. Karpinnen, M. Matvejeff, K. Salomaeki, H. Yamauchi, J. Mater. Chem. 12 (2002) 1761.

[32] H.M. Rietveld, J. Appl. Crystallogr. 2 (1969) 65.

[33] B.A. Hunter, 'Rietica–A Visual Rietveld Program" in Commission on Powder Diffraction Newsletter, 20 (1998) 21. Available at: http://www.iucr.org/iucr-top/comm/cpd/Newsletters/.

[34] H. Taguchi, J. Solid State Chem. 122 (1996) 297–302.

[35] J. Perez-Cacho, J. Blasco, J. Garcia, R. Sanchez, J. Solid State Chem. 150 (2000) 145–153.

[36] A. Mehta, R. Berliner, R.W. Smith, J. Solid State Chem. 130 (1997) 192–198.

[37] A. Kappatsch, A. Quezel-Ambrunaz, J. Sivardiere, J. Phys. 31 (1970) 369–376.

[38] H.W. Brinks, H. Fjellvag, A. Kjekshus, B.C. Hauback, J. Solid State Chem. 147 (1999) 464.

[39] W.T.A. Harrison, S.L. Hegwood, A.J. Jacobson, J. Chem. Soc. Chem. Commun. (1995) 1953–1954.

[40] V.G. Sathe, A.V. Pimpale, V. Siruguri, S.K. Paranjpe, J. Phys.: Condens. Matter 8 (1996) 3889.

[41] A. Mineshige, M. Inaba, T. Yao, Z. Ogumi, K. Kikuchi, M. Kawase, J. Solid State Chem. 121 (1996) 423.

[42] V.A. Cherepanov, Barkhatova, A.N. Petrov, V.I. Voronin, in: Proceedings of the Fourth International Symposium on Solid Oxide Fuel Cells (SOFC-IV), ECS Proceeding Series, Vol. 95-1, 1995, p. 434.

[43] H. Ohbayashi, T. Kudo, T. Gejo, Jpn. J. Appl. Phys. 13 (1974) 1.

[44] J. Kirchnerova, D.B. Hibbert, J. Mater. Sci. 28 (1993) 5800.

[45] M. Paraskevopoulos, J. Hemberger, A. Krimmel, A. Loidl, Phys. Rev. B 63 (2001) 224416/1.

[46] A. Krimmel, M. Reehuis, M. Paraskevopoulos, J. Hemberger, A. Loidl, Phys. Rev. B 64 (2001) 224404/1.

[47] S. Ya Istomin, J. Grins, G. Svensson, O.A. Drozhzhin, V.L. Kozhevnikov, E.V. Antipov, J.P. Attfield, Chem. Mater. 15 (21) (2003) 4012.

[48] D.J. Goossens, K.F. Wilson, M. James, Phys. Rev. B, 2003, submitted.

[49] R.D. Shannon, Acta Crystallogr. A 32 (1976) 751.